The Effect of Asymmetry in Abdominal Aortic Aneurysms Under Physiologically Realistic Pulsatile Flow Conditions

E. A. Finol
ASME Member, Research Assistant Professor,
Institute for Complex Engineered Systems,
Faculty, Biomedical Engineering
Carnegie Mellon University,
Pittsburgh, PA 15213

K. Keyhani
Staff Engineer,
Research and Development, Asyst Technologies,
Fremont, CA 94538

C. H. Amon
ASME Life Fellow,
Raymond J. Lane Distinguished Professor,
Mechanical Engineering, Biomedical
Engineering, and Institute for Complex
Engineered Systems,
Carnegie Mellon University,
Pittsburgh, PA 15213

In the abdominal segment of the human aorta under a patient's average resting conditions, pulsatile blood flow exhibits complex laminar patterns with secondary flows induced by adjacent branches and irregular vessel geometries. The flow dynamics becomes more complex when there is a pathological condition that causes changes in the normal structural composition of the vessel wall, for example, in the presence of an aneurysm. This work examines the hemodynamics of pulsatile blood flow in hypothetical three-dimensional models of abdominal aortic aneurysms (AAAs). Numerical predictions of blood flow patterns and hemodynamic stresses in AAAs are performed in single-aneurysm, asymmetric, rigid wall models using the finite element method. We characterize pulsatile flow dynamics in AAAs for average resting conditions by means of identifying regions of disturbed flow and quantifying the disturbance by evaluating flow-induced stresses at the aneurysm wall, specifically wall pressure and wall shear stress. Physiologically realistic abdominal aortic blood flow is simulated under pulsatile conditions for the range of time-average Reynolds numbers $50 \leqslant Re_m \leqslant 300$*, corresponding to a range of peak Reynolds numbers* $262.5 \leqslant Re_{peak} \leqslant 1575$*. The vortex dynamics induced by pulsatile flow in AAAs is depicted by a sequence of four different flow phases in one period of the cardiac pulse. Peak wall shear stress and peak wall pressure are reported as a function of the time-average Reynolds number and aneurysm asymmetry. The effect of asymmetry in hypothetically shaped AAAs is to increase the maximum wall shear stress at peak flow and to induce the appearance of secondary flows in late diastole.* [DOI: 10.1115/1.1543991]

Introduction

Abdominal Aortic Aneurysms (AAAs) occur in the infrarenal segment of the abdominal aorta, between the renal arteries and the iliac bifurcation. The majority of studies found in the medical literature report an increase in the incidence of aortic aneurysmal disease, which is expected in a continuously aging population in developed countries, since the likelihood of aneurysm development increases with age. There have been significant improvements in surgical procedures and technological advancements in imaging devices in the last decade, but the associated aneurysm mortality and morbidity rate have also risen concomitantly. The mean age of patients with AAA is 67 years and men are affected more than women by a ratio of 4:1 with prevalence up to 5 percent [1]. AAAs are a health risk of significant importance since they are largely asymptomatic until the onset of rupture, an event that carries an overall mortality rate of up to the 90 percent range. AAA rupture represents the 13th leading cause of death in the United States, causing more than 10,000 deaths each year [2] and affecting 1 in 250 individuals over 50 years of age. Therefore, the optimal strategy in the management of aneurysmal disease is opportunistic detection and prevention of aneurysm rupture.

Aneurysm rupture is a biomechanical phenomenon that occurs when the mechanical stress acting on the inner wall exceeds the failure strength of the diseased aortic tissue. Since the internal mechanical forces are initiated and maintained by the dynamic action of blood flow within the aneurysm, the *hemodynamics* of AAAs becomes an important element of study for the characterization of the biomechanical environment of aneurysms. The contribution of this paper is the study of axial and secondary flow patterns and their effect on wall pressure and wall shear stress distributions for hypothetical single-AAA asymmetric models simulating in-vivo pulsatile flow conditions. The effect of asymmetry is accounted for by evaluating the flow dynamics and the hemodynamic stresses in three-dimensional aneurysm geometries with varying degrees of asymmetry.

Aneurysm shapes may be saccular (balloon-like expansions of only a portion of the wall), fusiform (gradual dilation of the complete circumference of the artery), or cylindroid. The different shapes have not been related to any specific cardiovascular disease or clinical manifestation [3]. Additionally, it is unlikely that an aneurysm of medium or large size (diameter >4.5 cm) would be fusiform or axisymmetric. AAAs in an advanced stage of development are truly asymmetric, due to the presence of tissue surrounding the abdominal aorta and to the vertebral column located posterior to this artery segment. This makes a large AAA less fusiform and to grow apart from the lumen's centerline, accounting for a major anterior dilation and a more flat posterior surface. However, early numerical studies found in the literature are based on two-dimensional axisymmetric bulge models and most experimental studies on aneurysm flow visualization comprise in-vitro axisymmetric and asymmetric models.

Numerical investigations of blood flow in three-dimensional hypothetical AAA models are scarce in the literature. The first of their kind for steady and pulsatile flows was conducted by Taylor and Yamaguchi [4,5], who report the appearance and disappearance of a primary vortex and regions of high shear stresses both at the proximal and distal ends of the aneurysm. Steady flow results in double-aneurysm models indicate the existence of strong secondary flow patterns at the distal end [6]. Kumar et al. [7] report oscillatory flows for double-aneurysm models as a function of the Reynolds number and Strouhal number. Patient-specific AAA models have been used recently with rigid wall properties to simu-

Contributed by the Bioengineering Division for publication in the JOURNAL OF BIOMECHANICAL ENGINEERING. Manuscript received Feb. 2002; revised manuscript received Nov. 2002. Associate Editor: J. E. Moore, Jr.

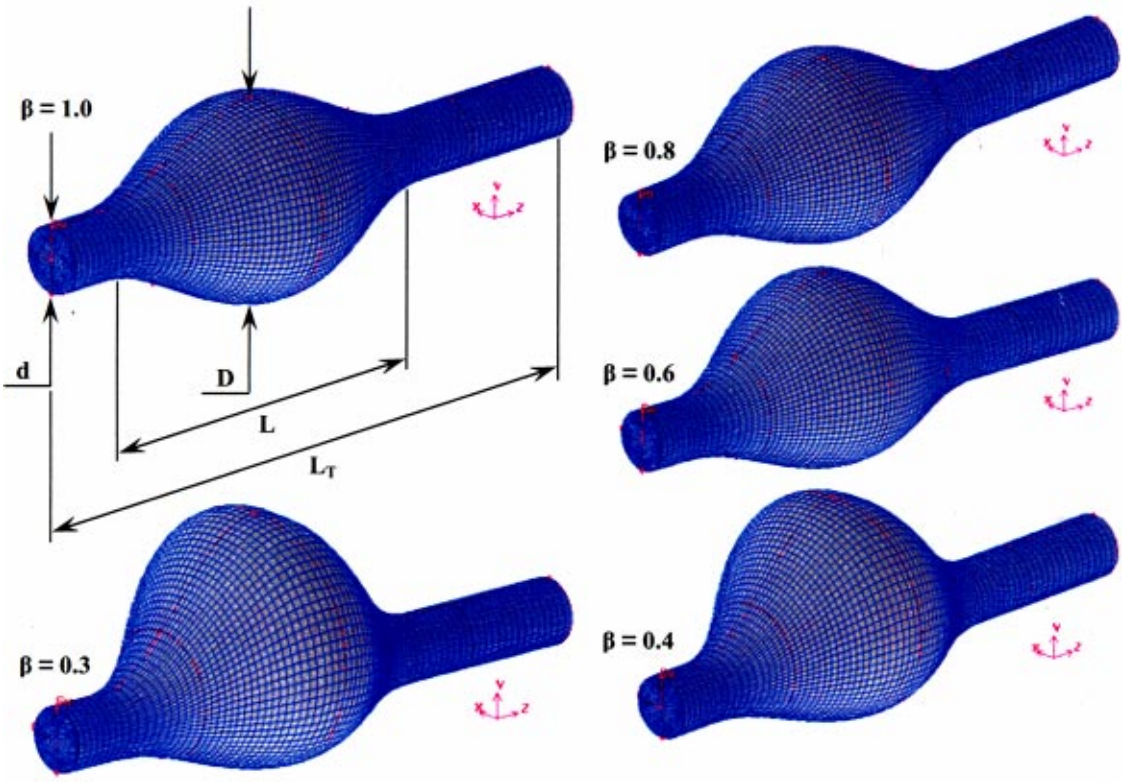

Fig. 1 Finite element discretization of three-dimensional AAA models, for which d=1.6 cm, D=3d, L=6d, and L_T=9.4d. A varying degree of asymmetry is considered for model #1-β=1.0 (axisymmetric), model #2-β =0.8, . . . , model #5-β=0.3.

late in-vivo pulsatile flow conditions [8]. Di Martino and colleagues [9–11] report the coupling of unsteady solid and fluid mechanics for the prediction of wall mechanical stresses and the estimation of an index of AAA rupture.

The investigation of experimental aneurysm hemodynamics is driven by the knowledge of boundary layer theory that flow separates and recirculates behind obstructions or expansions. Asbury et al. [12] and Peattie et al. [13] observed that wall pressure inside the aneurysm model reaches a maximum at the center and peak shear at the model exit is about 3.5 times greater than the mean shear at that section. Resting and exercise conditions were investigated experimentally resulting in three distinct flow regimes of pulsatile blood flow in AAAs [14,15]. Peattie and Bluth [16] suggest that aneurysm diameter has little effect on the wall pressure distribution and its magnitude over the pulsatile flow cycle. Recently, Atkinson et al. [17] and Feller et al. [18] measured flow patterns and wall shear stress for a range of instantaneous Reynolds numbers using patient-based AAA models obtained from spiral CT scans. Their contribution is the quantification of physiologically realistic pulsatile flow in the turbulent regime with patient-specific aneurysm geometries.

The role of fluid shear stresses in irregular geometries of large arteries regarding the onset of rupture is not completely understood. It is known that the vascular wall responds to disturbed flow conditions as recent studies demonstrate the existence of diverse endothelial cell responses under low levels of shear stress, but large *shear stress gradients*. Disturbed flow patterns at different levels of spatial shear stress gradients are found to trigger responses of the innermost layer of the tunica intima by altering intracellular flow-induced signaling in vascular endothelial cells [19–21].

Computational Modeling

Finite Element Models. Five single-aneurysm finite element models have been developed with various degrees of asymmetry and overall dimensions of: d=1.6 cm (typical diameter of a healthy human abdominal aorta [22,23]), D=3d, L=6d, L_T =9.4d, where d is the diameter of the undilated aorta. L_T is the total length of the vessel segment, which includes a short inflow length of 1.2 cm and an outflow length of 4.2 cm to account for the zero-traction outflow condition. Note that the maximum transverse dimension of each aneurysm is taken as three times the inlet diameter, or 4.8 cm. This would correspond to an aneurysm almost suitable for surgical repair, for which the critical diameter is generally taken as 5.0 cm [24]. Each corresponding finite-element computational domain is composed of 106,777 hexahedral linear elements, arranged in 96 layers in the axial direction for a total of 94,760 nodes. The software Gambit v1.3 (Fluent, Inc., Lebanon, NH) was used for the mesh generation. The exterior element faces of aneurysm models #1-5 are shown in Fig. 1, where the asymmetry parameter β is defined as the ratio of the maximum posterior and anterior wall dimensions [25].

Governing Equations and Boundary Conditions. Incompressible, homogeneous, Newtonian flow is simulated for average resting conditions at a heart rate of 60 bpm. Blood is a non-Newtonian suspension of cells in plasma, but it is reasonable to model it as a Newtonian fluid in vessels greater than approximately 0.5 mm in diameter [22]. The momentum and continuity equations in compact form are given by Eq. (1) as follows:

$$\frac{\partial \vec{\mathbf{V}}}{\partial t} = \vec{\mathbf{V}} \times \vec{\omega} - \nabla \tilde{\Pi} + \mathrm{Re}^{-1} \nabla^2 \vec{\mathbf{V}} \qquad (1a)$$

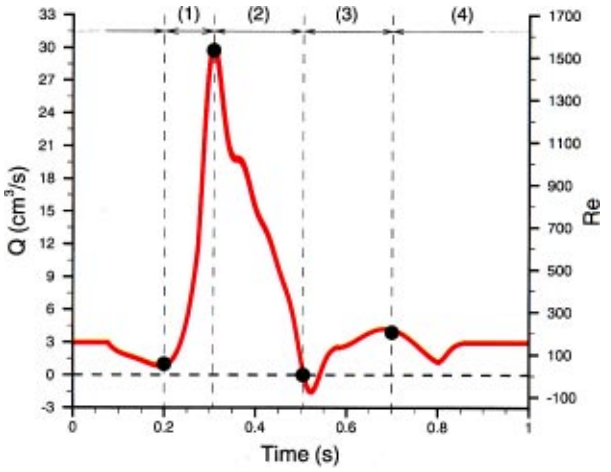

Fig. 2 Pulsatile volumetric flow rate (Q) and instantaneous Reynolds number (Re) for $Re_m=300$. Peak systolic flow occurs at t=0.31 s and diastolic phase begins at t=0.52 s. Flow phases (1) to (4) are described in the Flow Dynamics section.

$$\nabla\cdot\vec{\mathbf{V}}=0 \tag{1b}$$

where $\vec{\mathbf{V}}(\vec{r},t)=u_x\hat{i}+u_y\hat{j}+u_z\hat{k}$ is the velocity vector, $\vec{\omega}$ is the flow rotation tensor, and $\vec{\Pi}$ the fluid pressure. The stress components are determined using the Newtonian flow constitutive relationship, as given by Eq. (2), since incompressible flows satisfy the divergence-free condition for the velocity ($\nabla\cdot\mathbf{V}$):

$$\tau_{ij}=-p\delta_{ij}+\mu\left(\frac{\partial u_i}{\partial x_j}+\frac{\partial u_j}{\partial x_i}\right) \tag{2}$$

Details on the calculation of wall shear stress in three-dimensional geometries are given by Finol and Amon [26]. Blood flow is simulated for average blood properties: molecular viscosity $\mu=0.00319$ Pa·s and density $\rho=1{,}050$ kg/m^3. The governing equations are nondimensionalized by the inlet diameter and hemodynamic stresses evaluated at the wall are normalized using their corresponding magnitudes obtained for Poiseuille flow.

The boundary conditions for the velocity $\mathbf{V}$ are imposed as follows: (i) no-slip at the walls, (ii) fully developed paraboloid profile at the inlet, and (iii) stress-free outflow condition at the outlet. These are given in mathematical form by Eq. (3):

$$\vec{\mathbf{V}}=\vec{\mathbf{0}}\big|_{\text{wall}} \tag{3a}$$

$$u_z=2\bar{u}(t)\left[1-\left(\frac{2}{d}\right)^2(x^2+y^2)\right],\quad u_x=u_y=0\big|_{z=0} \tag{3b}$$

$$\tau_{ij}=-p\delta_{ij}+\mu\left(\frac{\partial u_i}{\partial x_j}+\frac{\partial u_j}{\partial x_i}\right)=0\big|_{z=L_T} \tag{3c}$$

For pulsatile flow, the inflow mean velocity is time-dependent and the volumetric flow rate is oscillatory, as shown in Fig. 2. The pulsatile waveform is represented by a discrete Fourier series based on the in-vivo measurement reported first by Mills et al. [27], which is a triphasic pulse appropriate for normal hemodynamic conditions in the abdominal segment of the human aorta. The curve is scaled to obtain a time-average Reynolds number $Re_m=300$, indicated by Pedersen and others [23] as acceptable for a patient in resting conditions. Maier et al. [28] have reported similar flow measurements in the normal abdominal aorta using ultrasound and magnetic resonance imaging. They indicate the existence of a longer time of flow reversal at the onset of diastole. The justification and choice among the flow waveforms measured by Mills and Maier is discussed in detail by Finol and Amon [29]. The Womersley number, which characterizes the flow frequency, the geometry and the fluid viscous properties, is $\alpha=11.5$. The amplitude coefficient of the waveform is $\gamma=5.25$ and peak systolic flow occurs at t=0.31 s. The time-average Reynolds number is calculated as $Re_m=d\bar{u}_m/\nu$, where $\bar{u}_m$ is the time-average inflow mean velocity.

Numerical Method. The governing equations are solved with the software Fidap v8.60 (Fluent, Inc., Lebanon, NH), which uses the finite element method (FEM) for the spatial discretization. The method is based on the Galerkin form of the method of weighted residuals, in which the solution of the governing equations is represented by a linear combination of unknown independent coefficients and polynomial functions over the entire computational domain, to obtain the discrete analog of the transport equations. Within each element of the domain, the transport variables are interpolated by functions of compatible order in terms of values to be determined at a set of nodes. For 8-node hexahedral (brick) elements, the variables are isoparametrically mapped using trilinear velocity approximations and piecewise constant discontinuous pressure approximations associated with the element centroid. The discrete form of the entire domain is obtained by the assemblage of all elements, such that the continuity of velocity between the elements is enforced, and the boundary conditions are satisfied. This discretization process results in a large non-linear set of equations that must be solved using iterative methods. Unlike the spectral-element method (SEM) used previously by Finol and Amon [30], the FEM employs linearly independent polynomial functions with respect to each Cartesian coordinate. For quadratic and higher-order elements, each element is subdivided into equally spaced nodal points in which the transport variables are evaluated.

For three-dimensional geometries, the initial-value code uses a segregated algorithm for solving the nonlinear system of matrix equations arising from the FEM discretization of the fluid flow equations. Thus, each conservation equation is solved separately in a sequential manner, avoiding the direct formation of a global system matrix. Alternatively, this matrix is decomposed into smaller sub-matrices that govern the nodal transport variables associated with only one conservation equation. The sub-matrices are then solved sequentially using iterative linear equation solvers, such as the conjugate gradient method for symmetric coefficient matrices and the conjugate gradient squared method for non-symmetric coefficient matrices. A pressure projection algorithm is utilized to obtain a solution for the velocity field at every iteration. The pressure projection version of the segregated algorithm, that has substantially reduced storage requirements compared to direct methods, is used to solve the non-linear system. The segregated solver creates a set of equations for a single degree of freedom at a time, and cycles sequentially through all unknowns at each iteration, thus avoiding the direct formation of a global system matrix. The linear sub-matrices associated with each field variable at every iteration of the algorithm, are also solved iteratively to further reduce storage requirement. The conjugate gradient squared and conjugate residual methods are used for the solution of the non-symmetric (velocity) and symmetric (pressure) linear sub-matrices respectively.

The time integration method used for the time dependent terms of the governing equations is the backward Euler method with a time step size (δt) of 0.008 seconds. Therefore, simulation results are obtained at 1/125 s intervals, but only selected flow stages considered to be the ones that represent the most important hemodynamic changes during the cardiac cycle are presented in this paper. These stages are obtained at the last cycle of the asymptotically converged time-periodic solution, which is reached after a transient resulting from the application of the initial condition. The applied initial condition (t=0) for the time integration is equivalent to the converged solution for constant flow at the flow rate obtained for t=0.

Mesh resolution tests and convergence studies were performed with several outflow lengths under conditions of constant flow

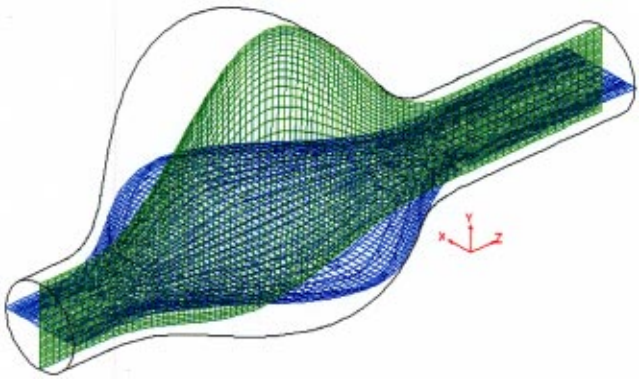

Fig. 3 Schematic of the transverse (x-z) and medial (y-z) planes used to evaluate the velocity field

rate, resulting in no significant changes in the flow patterns or shear stress distributions for outflow lengths greater than 2.5 inlet diameters. The workstations used to perform the simulations in this work typically had dual-pentium® III processors of 1.0 GHz clock speed, 1.0 GB RAM memory, and running on Linux Redhat® v7.1 operating system. The run time for a single simulation based on 5 consecutive pulsatile flow cycles was approximately 12 days of real time.

Results and Discussion

Five three-dimensional models are utilized to study the effect of varying the parameter β (asymmetry) in pulsatile flow hemodynamics of AAAs. These aneurysms are asymmetric with respect to the transverse (x-z) plane and the streamwise direction. At each cross-section, the medial (y-z) plane defines symmetry with respect to the left and right half surfaces. These two planes, as shown in Fig. 3, have been chosen to illustrate the velocity field at different stages of the cardiac cycle.

The numerical results are obtained at time-average Reynolds numbers over the range $50 \leqslant Re_m \leqslant 300$, for which the peak Reynolds number is obtained at $t=0.31$ s and varies over the range $262.5 \leqslant Re_{peak} \leqslant 1575$. The instantaneous Reynolds number, $Re(t_j)$, is based on the inflow mean velocity at time t_j. At the outlet section the viscous component of the stress is negligible and, therefore, the outflow boundary condition reduces to $p=0$ at the exit. Consequently, all the pressure results are relative to this value.

Flow Dynamics. Figures 4 and 5 illustrate velocity vectors within model #1 ($\beta=1.0$) and model #5 ($\beta=0.3$) for $Re_m=300$ at $t=0.20$ s, $t=0.30$ s, $t=0.42$ s, $t=0.52$ s, and $t=1.00$ s. The frames shown are visualizations of the projection of the three-dimensional velocity vector on the medial and transverse planes of each model. Since these planes are not completely parallel to and aligned with the faces of all the elements they intersect, careful consideration must be given to the discussion of the flow dynamics based on the projection of out-of-plane velocity components.

For all models, the residual vortices left from the previous cycle are present within the aneurysm until $t=0.08$ s. At this time, the flow is decelerated temporally until $t=0.20$ s, the stage at which there is a maximum growth of recirculation regions prior to the onset of systolic acceleration. Figure 4 shows that for the axisymmetric model at this stage there are four distinct low-velocity vortices in the converging end of the aneurysm at each plane. This results in two toroid-shaped vortices that loop around the core flow in ring-like shape. The proximal and distal ends are characterized by low negative velocities close to the wall, which are mainly due to convective effects as the flow accommodates to the change in geometry. In the first half of systole, a strong pressure gradient ejects the vortices downstream, as the flow accelerates concomitantly with time and reattaches to the wall. The maximum velocities and velocity gradients are obtained at peak flow, where a symmetric and streamlined flow pattern exists within the aneurysm model. Temporal deceleration combined with weak convective effects are the dominating factors in the second half of systole, where the high velocity jet gives away to significant hemodynamic disturbance, which initiates in the proximal end at $t=0.42$ s. At this stage, a symmetric ring vortex is shed off the wall at the point of flow separation while at the center and distal end there is a forward flow pattern. This description agrees qualitatively with.

As the flow reverses direction at $t=0.52$ s, the intensity of recirculating flow decreases, causing translation of the vortex center towards the centerline. This results in an extension of the wake of the vortex into the inlet section of the aneurysm. During diastole, the flow recovers its original direction with a moderate acceleration that yields translation of the main vortex towards the distal end and dissolution of the extended wake. The end of diastole is characterized by an almost constant flow rate and an intensification of the flow disturbance downstream due to local velocity increase.

The effect of aneurysm asymmetry in pulsatile flow dynamics is depicted in Fig. 5 for model #5 ($\beta=0.3$). The complex flow pattern observed for $t=0.20$ s near the exit of the aneurysm is intensified, with recirculation zones that extend to the proximal end. There is a region of forward flow that travels along the posterior wall while low-velocity retrograde flow shears the anterior wall in the absence of an orderly toroid-shaped vortex. At peak flow, a characteristic attached flow pattern is obtained throughout the aneurysm with nearly stagnant flow present along the anterior wall where the diameter is greatest. During systolic deceleration, flow separation occurs soon after peak flow and the ring vortex begins to travel downstream flattened by the posterior wall. The decrease in β is manifested by asymmetry of the ring vortex with respect to the z-axis, such that in the y-z plane at $t=0.42$ s two recirculation regions of different intensity and shape are obtained. The maximum negative velocity at this stage is 66 percent higher than for $\beta=1.0$, which gives an indication of the relative strength of recirculating flow. At $t=0.52$ s, the vortex is shed off the wall into the main stream where the flow coming from the exit decreases the intensity of the recirculation. The shape of the aneurysm in model #5 allows for the reversed flow to travel along the anterior wall and into the inflow region. The higher retrograde velocities obtained at this stage yield a faster forward flow in the wake of the vortex and at the centerline. Late diastole is depicted with significant and asymmetric flow recirculation near the aneurysm exit and negative velocities along the anterior wall.

A study of the magnitude and distribution of cross-streamwise velocities during the cardiac cycle for model #5 reveals that secondary flow patterns have a negligible effect on the vortex dynamics during systole. Conversely, secondary velocities influence the overall diastolic flow patterns, especially at those stages where temporal deceleration takes place or where the flow is dominated by convective deceleration. Figure 6 illustrates secondary velocity vectors at the midsection of the aneurysm, the proximal end and the distal end in model #5 at $t=0.20$ s (top row) and $t=1.00$ s (bottom row). While the proximal end of the aneurysm exhibits no significant secondary flow, two weak secondary vortices are obtained along the posterior wall at the midsection of the aneurysm for $t=0.20$ s. These vortices are responsible for the absence of a high-velocity jet of fluid along the z-axis, unlike steady flow and pulsatile-systolic flow patterns. The distal end exhibits velocities that shear the sides of the anterior and posterior walls in asymmetric fashion with higher velocities obtained at the anterior wall. The pattern supports previous results that high-velocity forward flow travels along the posterior wall, separating at the distal end and traveling in the opposite direction along the anterior wall [6].

At these stages of late diastole where the flow rate is either

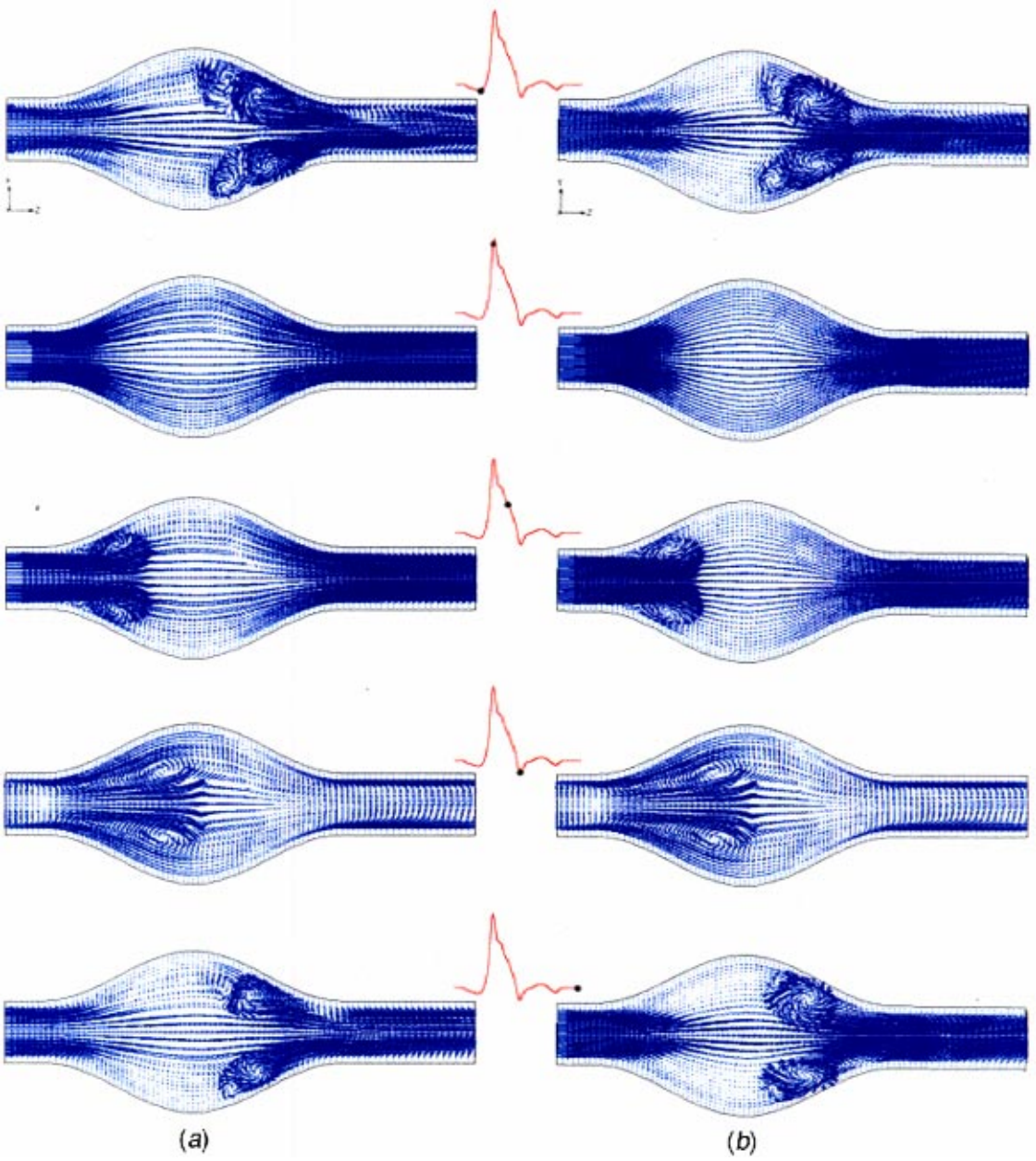

Fig. 4 Velocity vectors for Re_m=300 in model #1 (β=1.0) at different stages of the cardiac cycle (t=0.20, 0.30, 0.42, 0.52 and 1.00 s) for the (a) x-z plane and (b) y-z plane

constant or the pressure gradient is small, the increase in asymmetry results in a distal end where the walls of the aneurysm converge drastically and highly disturbed flow is obtained. The outward expansion of the anterior wall and the inward contraction of the posterior wall define the deviation of the aneurysm from its symmetric idealized shape (model #1). The deformed geometry allows more volume within the aneurysm sac for the flow to separate, recirculate slowly, and travel downstream following the slope defined by the posterior wall.

Based on the above description of AAA pulsatile flow, the following four flow phases summarize the aneurysm size dependent and asymmetry parameter dependent flow dynamics:

1. *Systolic acceleration* involves downstream ejection of the residual vortices left from the previous cycle, yielding an attached flow pattern.
2. *Systolic deceleration* is characterized by flow separation at the proximal end, toroid-shaped single-vortex growth and its translation downstream. The effect of asymmetry is to reduce the intensity of the vortex along the posterior wall, creating an asymmetric annular structure.
3. *Early diastole* is characterized by partial shedding of the vortex left from systole towards the main stream. Flow recirculation is reduced in size, as the centerline velocity increases in accord to the pressure gradient imposed by the inlet flow condition. Aneurysm asymmetry yields stronger velocity gradients along the anterior wall at the distal end.
4. *Late diastole* is the phase where the most significant flow disturbance takes place, largely influenced by the effect of secondary flows due to geometrical asymmetry. Disorganized recirculation regions that depart from the symmetric toroidal shape are present downstream of the aneurysm midsection until the onset of systolic acceleration in the next cardiac cycle.

These numerical results are in good qualitative agreement with

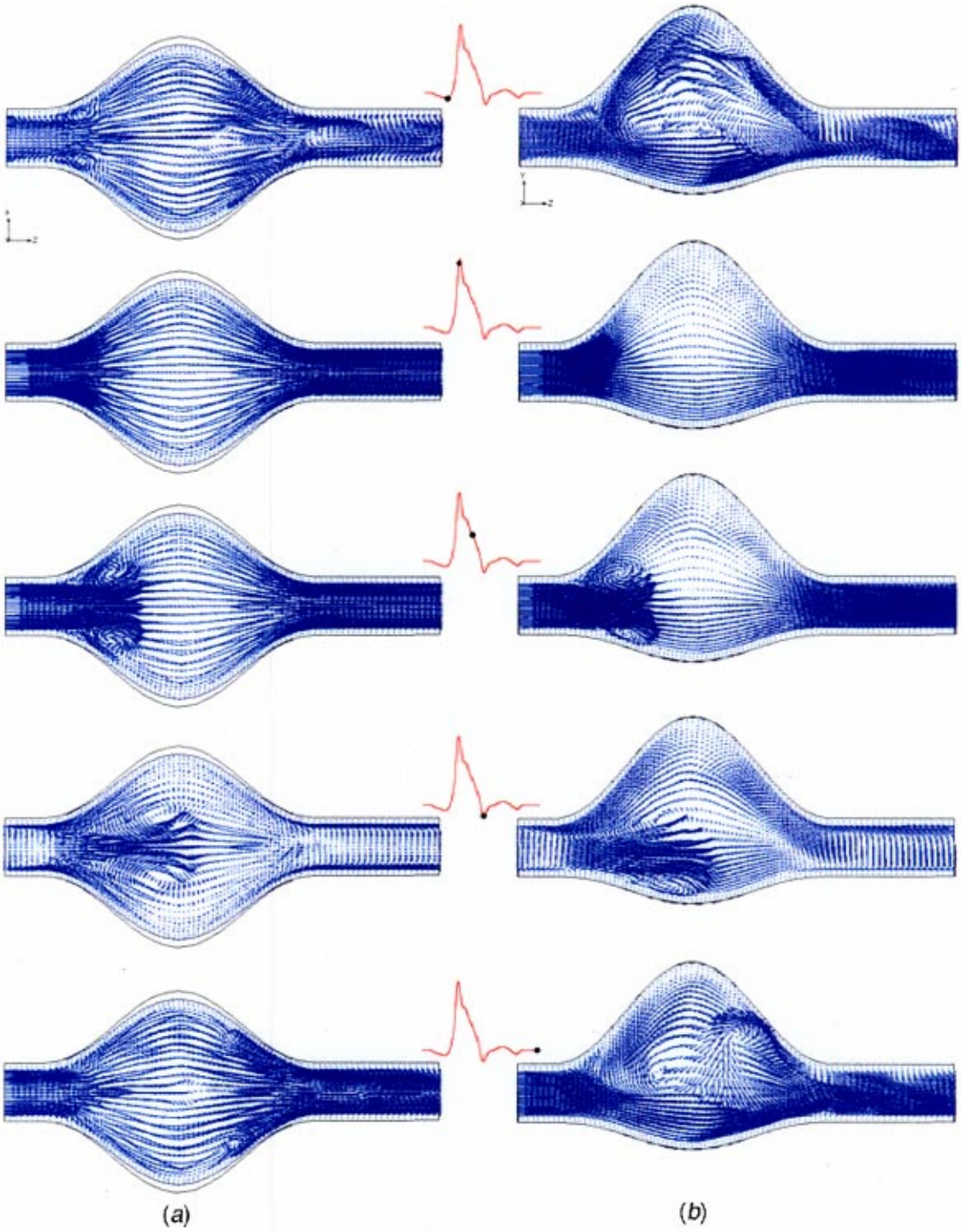

Fig. 5 Velocity vectors for $Re_m=300$ in model #5 ($\beta=0.3$) at different stages of the cardiac cycle (t=0.20, 0.30, 0.42, 0.52 and 1.00 s) for the (a) x-z plane and (b) y-z plane

flow visualizations available in the literature [14,15]. The possibility of detecting transition to turbulence in asymmetric AAAs is also addressed in this work. The peak Reynolds number in Fig. 2 is 1575, which is below the critical Reynolds number of 2300 for smooth pipe flows. Other investigators have been unable to visualize transition to turbulence in experimental flow studies in the abdominal aorta under average resting conditions [23] or in moderately sized AAAs for up to $Re_{peak}=3308$ and D=2.1d [14]. They claim that a transitional regime exists for certain flow stages at medium exercise conditions and a vortex ring bursting into turbulence is expected in late diastole for exercise conditions [15]. Furthermore, we utilized the same flow waveform and simulated the same range of time-average Reynolds numbers in two-dimensional axisymmetric bulge models [31] without detecting a temporal transition to turbulence. Using spectral elements for the direct numerical simulation of transitional flows in complex geometries [32], we have not captured any numerical instabilities or singularities for time-dependent flow conditions that would indicate a transient turbulence.

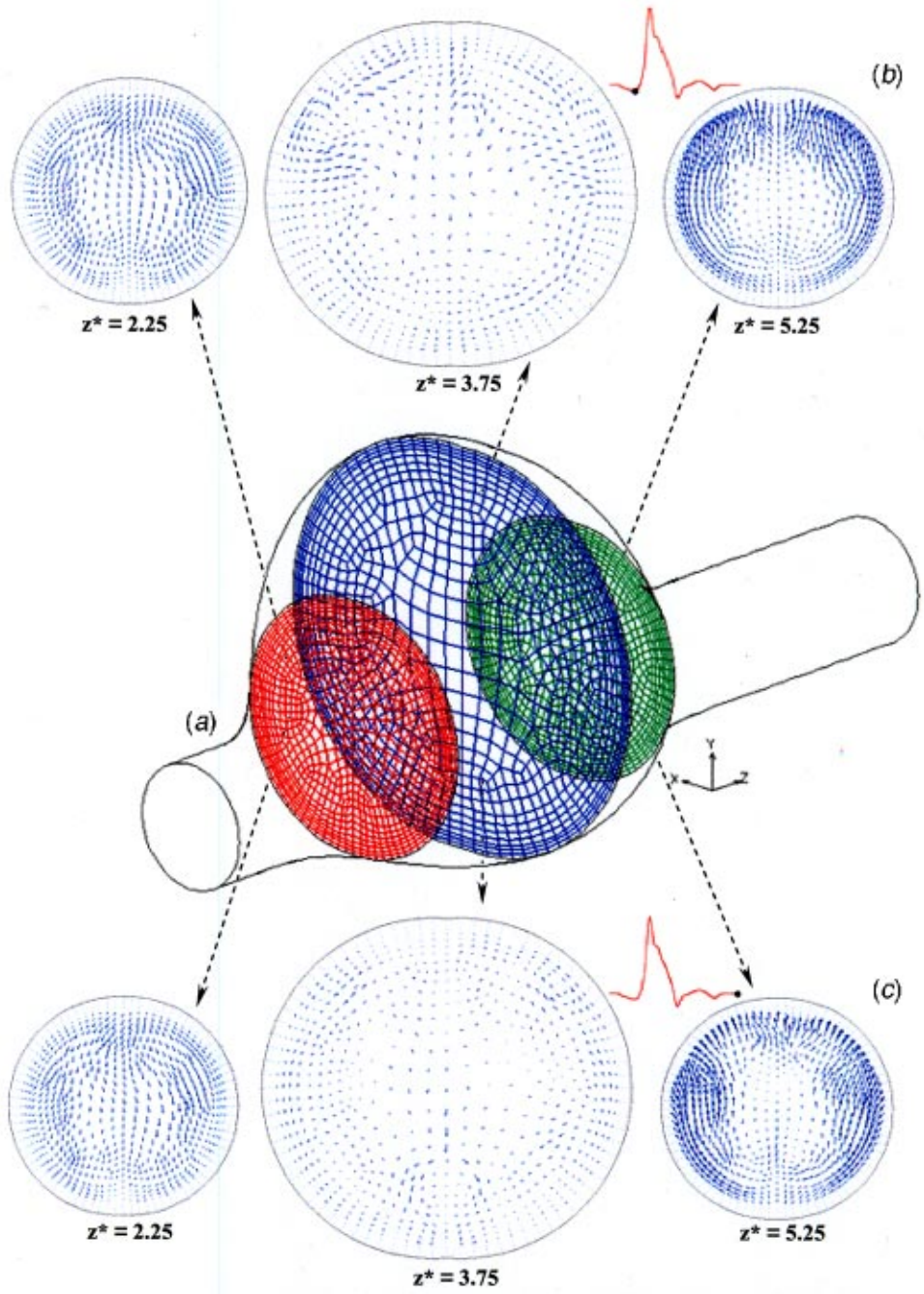

Fig. 6 Cross-streamwise velocity vectors for $Re_m=300$ at the proximal end, midsection and distal end of model #5 ($\beta=0.3$); (a) location of selected cross-sections, (b) vectors for t=0.20 s and (c) vectors for t=1.00 s

Hemodynamic Wall Pressure. Spatial changes in the dynamic pressure component at any given stage of the flow during the cardiac cycle are found to be very small along the aneurysm wall, a result previously obtained by Elger et al. [33] for two-dimensional axisymmetric AAA models. The most significant pressure change is obtained prior to peak flow, at t=0.29 s, where the pressure gradient is greatest. The wall pressure distribution at t=0.29 s along the anterior wall of models #1, #3 and #5 is shown in Fig. 7. Within the aneurysm, wall pressure is almost uniform, decreasing slightly downstream towards the distal end, which is produced by the change of cross-sectional area imposed by the outlet extension. In general, the variation in hemodynamic wall pressure from inlet to exit follows the trend imposed by the pressure gradient that results from the application of the pulsatile flow inlet boundary condition.

Wall Shear Stress. Figures 8 and 9 illustrate surface distributions of the magnitude of normalized shear stress at the inner wall of model #1 ($\beta=1.0$), model #3 ($\beta=0.6$) and model #5 ($\beta=0.3$) for $Re_m=300$ at t=0.20 s and t=0.30 s, respectively. Wall shear stress in each aneurysm is normalized by the Poiseuille flow wall shear stress for the same time-average flow rate of the cardiac pulse. Equation 4 defines the normalized wall shear stress at any location $\vec{r}(x,y,z)$ and time t:

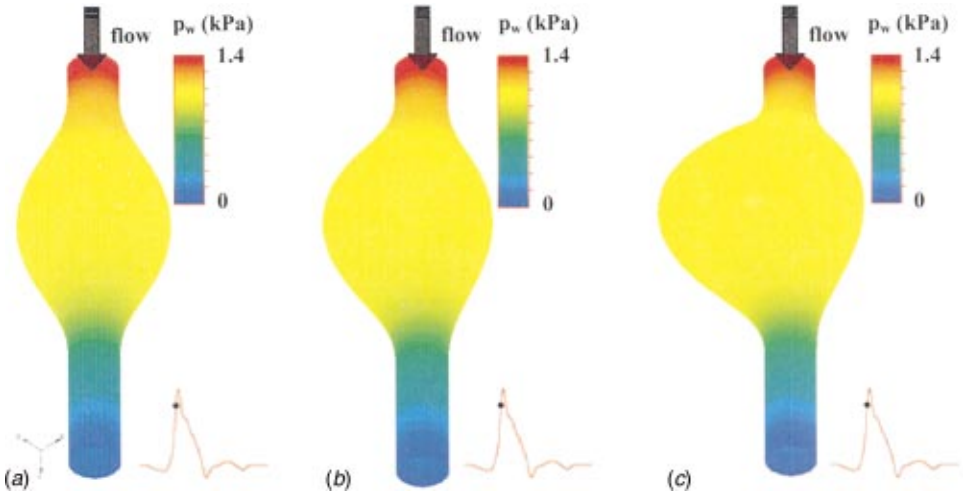

Fig. 7 Wall pressure surface distributions for Re_m=300 at t=0.29 s in (a) model #1-β=1.0, (b) model #3-β=0.6 and (c) model #5-β=0.3.

$$\tau_w^*(\bar{r},t)=\frac{\tau_w(\bar{r},t)}{\tau_{wo}};\qquad \tau_{wo}=\frac{8}{\rho}\left(\frac{\mu}{d}\right)^2 Re_m \tag{4}$$

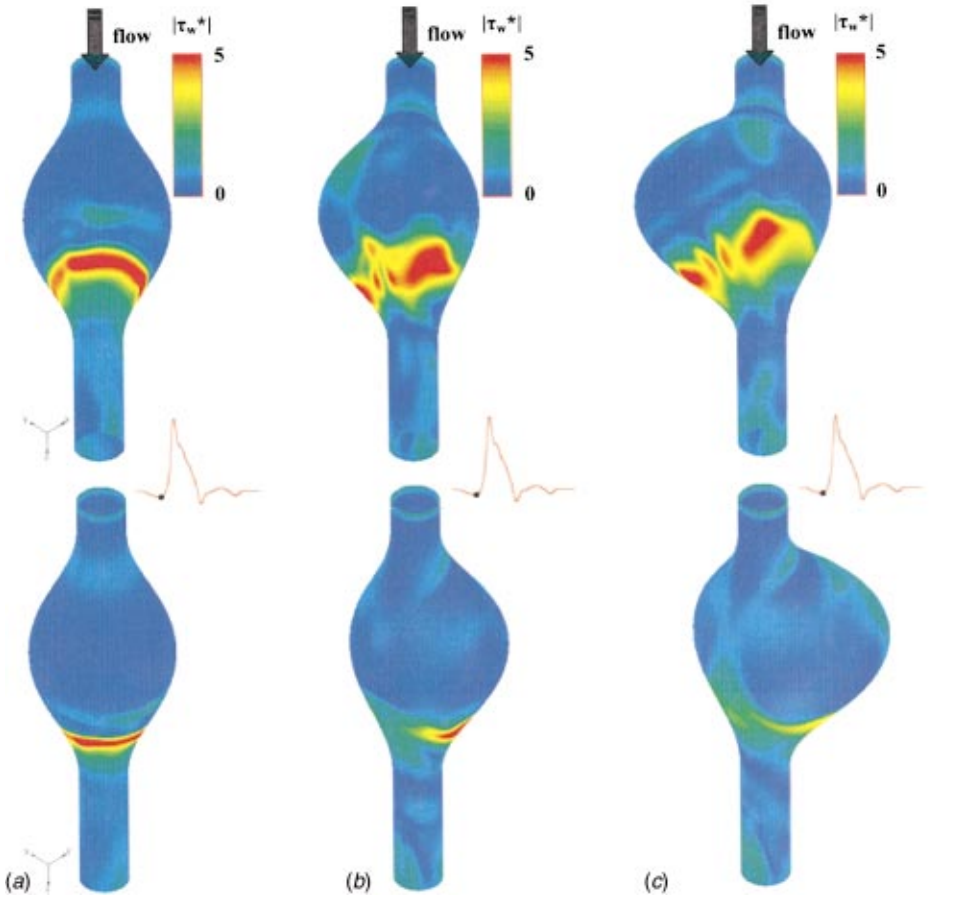

Fig. 8 Wall shear stress surface distributions for Re_m=300 at t=0.20 s in (a) model #1-β=1.0, (b) model #3-β=0.6 and (c) model #5-β=0.3

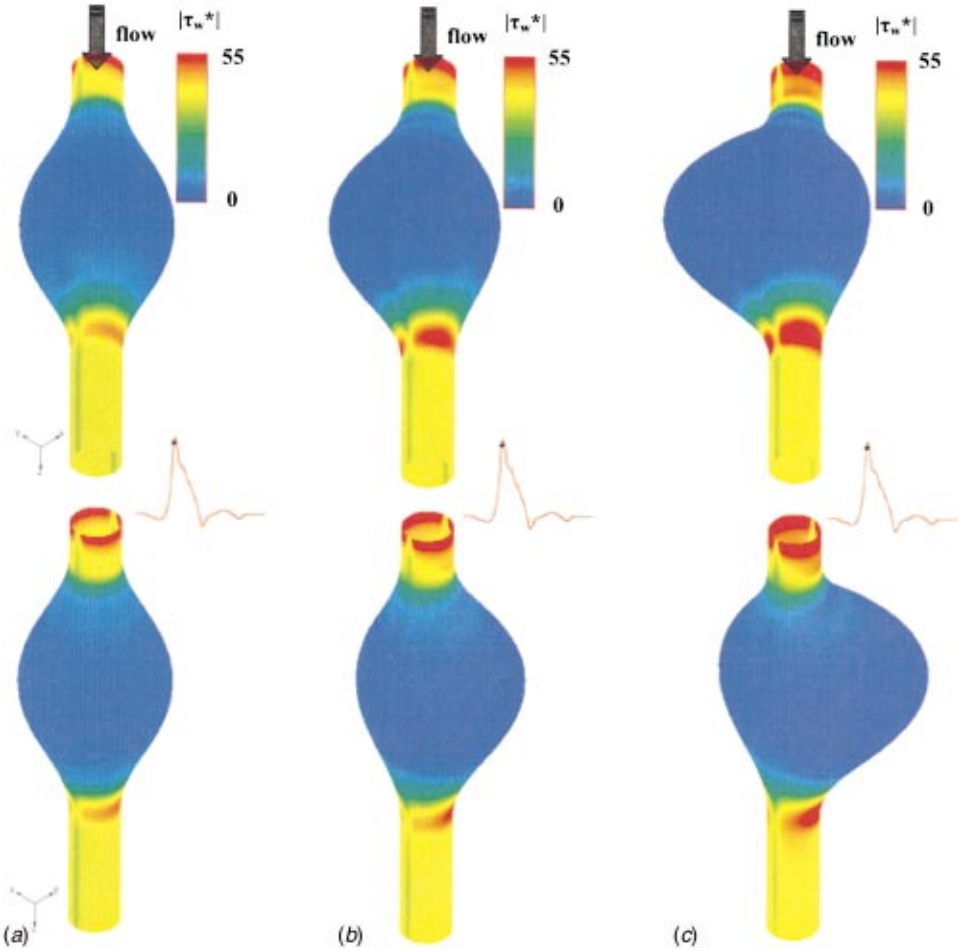

Fig. 9 Wall shear stress surface distributions for Re_m=300 at t=0.30 s in (a) model #1-β=1.0, (b) model #3-β=0.6 and (c) model #5-β=0.3

$$\tau_w^*(\vec{r},t)=\frac{\tau_w(\vec{r},t)}{\tau_{wo}};\quad \tau_{wo}=\frac{8}{\rho}\left(\frac{\mu}{d}\right)^2 Re_m \tag{4}$$

At t=0.20 s, the wall shear stress distribution for average resting conditions is shown in Fig. 8 depicting the anterior wall view (top row) and the posterior wall view (bottom row) for the fixed scale of 0 to 5. The direction of the flow is from top to bottom. At this stage, where the pulsatile velocity curve is at an inflexion point and a moderate deceleration of the flow has taken place, the wall shear stress is complexly distributed, in particular where the wall converges into the outflow section. For model #1, symmetry and uniformity in wall shear stress is achieved from the entrance to the center of the aneurysm. Downstream of the midsection, the distal end is characterized by symmetric flow patterns and recirculation regions that induce nonuniform velocity gradients and a significant increase in wall shear stress. This flow disturbance differentiates the end of diastole from systole, as the residual vortices from the previous pulsatile cycle remain within the aneurysm at the onset of the new pulse. The result is that the maximum normalized wall shear stress [$\tau^*_{w,max}$ (t=0.20 s)] is consistently obtained along the lateral-anterior wall at the distal end of the aneurysm for all models illustrated in Fig. 8. Within the dilated portion of the vessel this stress varies between 5.4 and 5.7, suggesting that at an early stage of the cardiac cycle defined by t=0.20 s, the maximum wall shear stress in an aneurysm of hypothetical shape may be up to 5.7 times the wall shear stress expected for a normal abdominal aorta under the same blood flow conditions. For models #3 and #5, the forward flow that travels along the posterior wall yields a nonuniform wall shear stress distribution, the highest value of which is obtained downstream of the aneurysm midsection.

The maximum wall shear stress during the pulsatile cycle is obtained at peak flow, where the velocities and their spatial gradients are greatest, as seen in Fig. 9, for which the fixed scale of the wall shear stress is 11 times greater than in Fig. 8. The completely attached flow pattern obtained at t=0.30 s yields positive wall shear stress from the inlet to outlet regions and a pattern that is approximately uniform at each vessel cross-section, even for the asymmetric models (#3 and #5). This uniformity is obtained along both the posterior and anterior walls. Ignoring the entrance effect caused by imposition of the fully-developed inlet condition, the maximum wall shear stress at peak flow is always obtained just upstream of the outflow section of the aneurysm. This is a region where the pathlines of the velocity field contract as convective acceleration dominates the flow to satisfy mass conservation. As the aneurysm becomes more asymmetric, the maximum shear stress increases concomitantly. For β=1.0, the normalized maximum wall shear stress at t=0.30 s [$\tau^*_{w,max}$ (t=0.30 s)] within the dilated portion of the vessel is 47.1; for β=0.6 it is 51.4 and for β=0.3 it is 60.4. This indicates that there is a remarkable increase in wall shear stress from a normal aorta to a dilated one at the stage where peak flow is achieved. Additionally, the maximum wall shear stress escalates by 27 percent from the axisymmetric model (β=1.0) to the most asymmetric one (β=0.3).

Pulsatile Flow Correlations. Figure 10 illustrates the varia-

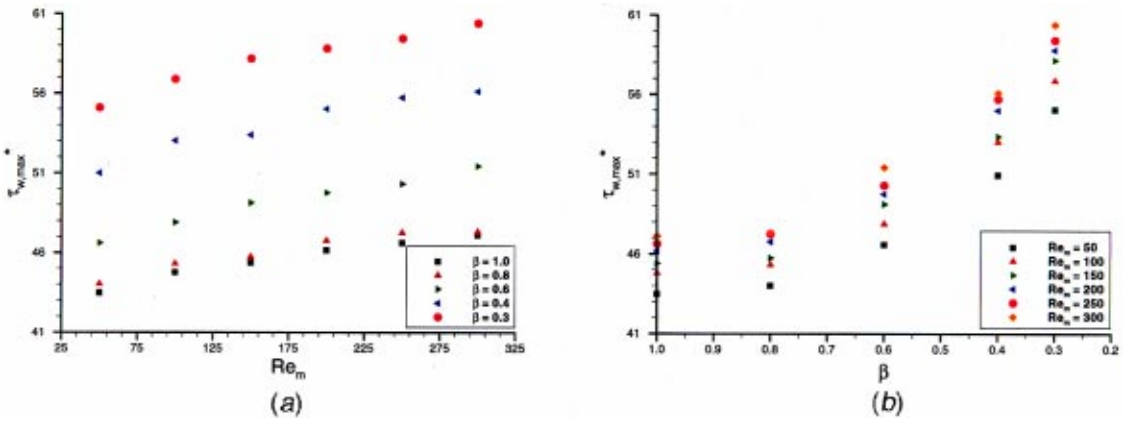

Fig. 10 Dependence of maximum wall shear stress on (a) time-average Reynolds number and (b) asymmetry parameter, at peak flow

tion of maximum wall shear stress at peak flow as a function of the time-average Reynolds number and degree of asymmetry. A common trend is obtained for which $\tau^*_{w,max}$ (peak) increases proportionally with Re_m and inversely proportional to β. Based on a normalization by Poiseuille flow at a flow rate obtained for each time-average Reynolds number simulated, the increase in the peak wall shear stress for the pulsatile cycle is almost negligible between models #1 (axisymmetric) and #2 (moderate asymmetry). Furthermore, the variation of shear stress with β is nonlinear, as the differential in maximum wall shear stress becomes greater with increasing asymmetry. Since the flow pattern at peak flow is characterized by the absence of separation and recirculation for all AAA models under study, the comparison of the relative magnitude of flow-induced stresses at the wall is solely based on the ''ability'' of the geometry to yield large velocity gradients at the distal end of the aneurysm. Therefore, the discussion that supports the trend of variation of maximum wall shear stress with Re_m and β has its basis on the evolution of the aneurysm as the anterior wall expands outwardly. With this expansion, the volume of blood flow the aneurysm is capable of enclosing between the normal lumen of the aorta and the anterior wall increases greatly, as the posterior wall contracts inward providing a smoother surface where local changes in fluid stresses near the wall become increasingly smaller. For the levels of volumetric flow rate that Mills' pulsatile waveform [27] is scaled to $Re_m = 300$, there will be a value of asymmetry for which the exponential increase in maximum wall shear stress can no longer be sustained by an attached flow pattern. Thus, it is expected that for aneurysms that are more asymmetric than model #5, the smooth streamlined pattern previously achieved at peak flow may not be attainable and early flow recirculation regions will appear next to the anterior wall of the AAA. The projected result is that the almost linear increase of maximum shear stress with Re_m and the exponential increase with β are disrupted, as negative shear stresses will be present along the anterior wall.

Conclusions

Finite element numerical simulations of unsteady, incompressible, Newtonian blood flow in three-dimensional rigid models of single aneurysms have been presented. This work has investigated axial and secondary flow patterns and their effect on flow-induced stresses at the AAA wall for physiologically realistic pulsatile blood flow rates.

The vortex dynamics is characterized by means of a sequence of different flow stages in one period of the cardiac pulse. The following four phases illustrate the flow dynamics, which is dependent on the size of the aneurysm and its asymmetry: (i) systolic acceleration, (ii) systolic deceleration, (iii) early diastole, and (iv) late diastole. The effect of geometrical asymmetry is to induce asymmetric annular vortices and forward flow jets that shear the posterior wall of the aneurysm. The time-dependent pressure gradient that results from the pulsatile inlet boundary condition drives the flow dynamics. Additionally, the flow-induced pressure along the inner wall of the aneurysm is distributed according to this pressure gradient. However, aneurysm shape and asymmetry do not yield large normal forces on the wall or significant nonuniform pressures, resulting in small wall pressure variations within the dilated portion of the vessel segment.

The temporal evolution of the axial flow and the secondary flow patterns during diastole influence the spatial and temporal distribution of wall shear stresses. At peak flow, the highest wall shear stresses are obtained at the distal end of each aneurysm model utilized in the present study. The peak wall shear stress for average resting hemodynamic conditions varies with the degree of aneurysm asymmetry and is between 47 and 60 times higher than the corresponding wall shear stress obtained for a normal aorta at the same time-average flow rate. Therefore, the effect of asymmetry is to increase the wall shear stress downstream of the aneurysm midsection.

The study of flow hemodynamics without the interaction of the compliant wall of the aneurysm provides insight into the complexity of the vortex dynamics originated by the application of fluid boundary conditions combined with hypothetical geometries of asymmetric aneurysms. It is unknown, however, what is the potential role of spatial- or time-varying wall shear stresses in AAA pathophysiology or with regards to the onset of rupture. Additionally, an adequate criterion has not been presented for estimating AAA dynamic flow-induced stresses, since wall mechanics is not accounted for in the simulation of the momentum transport equations with rigid vessel walls. Further investigation is required by developing three-dimensional wall-compliant asymmetric computational models in which both hemodynamics and wall mechanics are computed. These models could be used for numerical simulations of pulsatile flow with wall interaction to estimate the inner wall mechanical stresses induced by the flow. Therefore, the results presented in this paper serve as preliminary predictions for the results expected from large-scale simulations utilizing three-dimensional wall-compliant modeling of aneurysms.

Acknowledgments

The authors gratefully acknowledge the financial support of the National Science Foundation grant CTS-9630801, the Whitaker Foundation grant RG-96-0202, and the Pennsylvania Infrastructure Technology Alliance (PITA) from the Commonwealth of Pennsylvania's Department of Community and Economic Development.

References

[1] Karkos, C., Mukhopadhyay, U., Papakostas, I., Ghosh, J., Thomson, G., and Hughes, R., 2000, ''Abdominal Aortic Aneurysm: the Role of Clinical Examination and Opportunistic Detection,'' Eur. J. Vasc. Endovasc Surg., **19**, pp. 299–303.

[2] Gillum, R., 1995, ''Epidemiology of Aortic Aneurysm in the United States,'' J. Clin. Epidemiol., **48**, pp. 1289–1298.

[3] Cotran, R., Kumar, V., and Collins, T., 1999, ''Robbins Pathologic Basis of Disease,'' 6th Edition, W. B. Saunders Company, Philadelphia, PA, pp. 524–546.

[4] Taylor, T., and Yamaguchi, T., 1992, ''Three-Dimensional Simulation of Blood Flow in an Abdominal Aortic Aneurysm using Steady and Unsteady Computational Methods,'' *1992 Advances in Bioengineering*, ASME BED-**22**, pp. 229–232.

[5] Taylor, T., and Yamaguchi, T., 1994, ''Three-Dimensional Simulation of Blood Flow in an Abdominal Aortic Aneurysm—Steady and Unsteady Flow Cases,'' ASME J. Biomech. Eng., **116**, pp. 89–97.

[6] Finol, E., and Amon, C., 2001, ''Secondary Flow and Wall Shear Stress in Three-Dimensional Steady Flow AAA Hemodynamics,'' *2001 Advances in Bioengineering*, ASME BED-**51**, IMECE2001/BED-23013.

[7] Kumar, R., Yamaguchi, T., Liu, H., and Himeno, R., 2001, ''Numerical Simulation of 3D Unsteady Flow Dynamics in a Blood Vessel with Multiple Aneurysms,'' *2001 Advances in Bioengineering*, ASME BED-**50**, pp. 475–476.

[8] Finol, E., Amon, C., Di Martino, E., and Vorp, D., 2002, ''Pressure and Wall Shear Stress Distribution in Abdominal Aortic Aneurysms: Patient-Specific Modeling,'' in *Computer Methods in Biomechanics and Biomedical Engineering*, 4th Edition, ed. by J. Middleton, M. Jones, N. Shrive, and G. Pande, Gordon and Breach Science Publishers, Newark, NJ, *in press*.

[9] Di Martino, E., Guadagni, G., Fumero, A., Spirito, R., and Redaelli, A., 2001, ''A Computational Study of the Fluid-structure Interaction within a Realistic Aneurysmatic Vessel Model obtained from CT Scans Image Processing,'' in *Computer Methods in Biomechanics and Biomedical Engineering*, 3rd Edition, ed. by J. Middleton, M. Jones, N. Shrive, and G. Pande, Gordon and Breach Science Publishers, Newark, NJ, pp. 719–724.

[10] Di Martino, E., Guadagni, G., Corno, C., Fumero, A., Spirito, R., Biglioli, P., and Redaelli, A., 2001, ''Towards an Index Predicting Rupture of Abdominal Aortic Aneurysms,'' *2001 Advances in Bioengineering*, ASME BED-**50**, pp. 821–822.

[11] Di Martino, E., Guadagni, G., Fumero, A., Ballerini, G., Spirito, R., Biglioli, P., and Redaelli, A., 2001, ''Fluid-structure Interaction within Realistic Three-dimensional Models of the Aneurysmatic Aorta as a Guidance to Assess the Risk of Rupture of the Aneurysm,'' Med. Eng. Phys., **23**, pp. 647–655.

[12] Asbury, C., Ruberti, J., Bluth, E., and Peattie, R., 1995, ''Experimental Investigation of Steady Flow in Rigid Models of Abdominal Aortic Aneurysms,'' Ann. Biomed. Eng., **23**, pp. 29–39.

[13] Peattie, R., Bluth, E., Ruberti, J., and Asbury, C., 1996, ''Steady Flow in Models of Abdominal Aortic Aneurysms—Part I: Investigation of Velocity Patterns,'' J. Ultrasound Med., **15**, pp. 679–688.

[14] Egelhoff, C., Budwig, R., Elger, D., and Khraishi, T., 1997, ''A Model Study of Pulsatile Flow Regimes in Abdominal Aortic Aneurysms,'' *Proceedings of the 1997 ASME Fluids Engineering Division Summer Meeting*, ASME FED-**21**, pp. 1–8.

[15] Egelhoff, C., Budwig, R., Elger, D., Khraishi, T., and Johansen, K., 1999, ''Model Studies of the Flow in Abdominal Aortic Aneurysms during Resting and Exercise Conditions,'' J. Biomech., **32**, pp. 1319–1329.

[16] Peattie, R., and Bluth, E., 1998, ''Experimental Study of Pulsatile Flows in Models of Abdominal Aortic Aneurysms,'' *Proceedings of the 20th Annual International Conference of the IEEE Engineering in Medicine and Biology Society*, **20**, pp. 367–370.

[17] Atkinson, S., Feller, K., and Peattie, R., 2001, ''Measurement of Fluid Flow Patterns and Wall Shear-Stresses in Patient-Based Models of Abdominal Aortic Aneurysms,'' *2001 Advances in Bioengineering*, ASME BED-**50**, pp. 753–754.

[18] Feller, K., Atkinson, S., and Peattie, R., 2001, ''Quantification of Flow Stability in Patient-Based Models of Abdominal Aortic Aneurysms,'' *2001 Advances in Bioengineering*, ASME BED-**50**, pp. 729–730.

[19] Satcher, R., Bussolari, S., Gimbrone, M., and Dewey, C., 1992, ''The Distribution of Forces on Model Arterial Endothelium Using Computational Fluid Dynamics,'' ASME J. Biomech. Eng., **114**, pp. 309–316.

[20] DePaola, N., Gimbrone, M., Davies, P., and Dewey, C., 1992, ''Vascular Endothelium Responds to Fluid Shear Stress Gradients,'' Arterioscler. Thromb., **12**, pp. 1254–1257.

[21] Davies, P., Mundel, T., and Barbee, K., 1995, ''A Mechanism for Heterogeneous Endothelial Responses to Flow In Vivo and In Vitro,'' J. Biomech., **28**, pp. 1553–1560.

[22] Milnor, W., 1989, ''Hemodynamics,'' 2nd Edition, Williams and Wilkins, Baltimore, MD, pp. 34–35.

[23] Pedersen, E., Sung, H., Burlson, A., and Yoganathan, A., 1993, ''Two-dimensional Velocity Measurements in a Pulsatile Flow Model of the Normal Abdominal Aorta simulating different Hemodynamic Conditions,'' J. Biomech., **26**, pp. 1237–1247.

[24] Hassen-Khodja, R., Sala, F., Bouillanne, P., Declemy, S., Staccini, P., and Batt, M., 2001, ''Impact of Aortic Diameter on the Outcome of Surgical Treatment of Abdominal Aortic Aneurysm,'' Ann. Vasc. Surg., **15**, pp. 136–139.

[25] Vorp, D., Raghavan, M., and Webster, M., 1998, ''Mechanical Wall Stress in Abdominal Aortic Aneurysm: Influence of Diameter and Asymmetry,'' J. Vasc. Surg., **27**, pp. 632–639.

[26] Finol, E., and Amon, C., 2000, ''On the Calculation of Fluid Shear Stresses at the Wall of Dilated Large Arteries: Part II—Application to 3D Computational Models,'' *2000 Advances in Bioengineering*, ASME BED-**48**, pp. 13–14.

[27] Mills, C., Gabe, I., Gault, J., Mason, D., Ross, J., Jr., Braunwald, E., and Shillingford, J., 1970, ''Pressure-flow Relationships and Vascular Impedance in Man,'' Cardiovasc. Res., **4**, pp. 405–417.

[28] Maier, S., Meier, D., Boesiger, P., Moser, U., and Vieli, A., 1989, ''Human Abdominal Aorta: Comparative Measurements of Blood Flow with MR Imaging and Multigated Doppler US,'' Radiology, **171**, pp. 487–492.

[29] Finol, E., and Amon, C., 2001, ''Blood Flow in Abdominal Aortic Aneurysms: Pulsatile Flow Hemodynamics,'' ASME J. Biomech. Eng., **123**, pp. 474–484.

[30] Finol, E., and Amon, C., 2002, ''Flow-Induced Wall Shear Stress in Abdominal Aortic Aneurysms: Part I—Steady Flow Hemodynamics,'' Computer Methods in Biomechanics and Biomedical Engineering, **5**(4), pp. 309–318.

[31] Finol, E., and Amon, C., 2002, ''Flow-Induced Wall Shear Stress in Abdominal Aortic Aneurysms: Part II—Pulsatile Flow Hemodynamics,'' Computer Methods in Biomechanics and Biomedical Engineering, **5**(4), pp. 319–328.

[32] Amon, C., 1993, ''Spectral Element-Fourier Method for Transitional Flows in Complex Geometries,'' AIAA J., **31**, pp. 42–48.

[33] Elger, D., Slippy, J., Budwig, R., Khraishi, T., and Johansen, K., 1995, ''A Numerical Study of the Hemodynamics in a Model Abdominal Aortic Aneurysm (AAA),'' *Proceedings of the ASME Symposium on Biomedical Fluids Engineering*, ed. by R. Gerbsch and K. Ohba, ASME FED-**212**, pp. 15–22.